

## Supporting Information

# Unveiling $\pi$ - $\pi$ interactions in triptycene-phenazine/SWCNT redox chemistry using ESR spectroscopy

Qi Chen,<sup>1</sup> Rie Suizu,<sup>1</sup> Yoshiaki Shuku,<sup>1</sup> Haruka Omachi,<sup>1</sup> Michio M. Matsushita,<sup>1</sup> Shuta Fukuura,<sup>3</sup>  
Takashi Yumura,<sup>3</sup> Shunji Bandow,<sup>2</sup> and Kunio Awaga<sup>1, \*</sup>

1. Department of Chemistry, Nagoya University, Furo-cho, Chikusa-ku, Nagoya, Aichi 464-8602, Japan
2. Department of Applied Chemistry, Meijo University, 1-501 Shiogamaguchi, Tenpaku-ku, Nagoya, Aichi 468-8502, Japan
3. Faculty of Materials Science and Engineering, Graduate School of Science and Technology, Kyoto Institute of Technology, Matsugasaki, Sakyo-ku, Kyoto 606-8585, Japan

\* Corresponding author.

E-mail address: [awaga.kunio.h8@f.mail.nagoya-u.ac.jp](mailto:awaga.kunio.h8@f.mail.nagoya-u.ac.jp) (K. Awaga)

## Table of Contents:

### S1. Preparation and Characterization of Trip-Phz/SWCNT

S1.1 Sample preparation

S1.2 TEM images

S1.3 FTIR spectra

### S2. Cyclic Voltammograms in Solution

S2.1 Neutral DMSO

S2.2 Acidic DMSO

S2.3 Acidic ACN

### S3. Solid-State Electrochemistry

S3.1 Ratio dependent CV curves

S3.2 Three component contributions

S3.3 Electrochemical impedance spectroscopy

S3.4 Charge-discharge profiles

### S4. DFT Calculation

S4.1 Interatomic separation

S4.2 Stabilization energy

### S5. Physical Properties

S5.1 Electronical conductivity

S5.2 Magnetic susceptibility

### S6. Electron Spin Resonance

S6.1 ESR lineshape analysis

S6.2 Determination of spin concentration

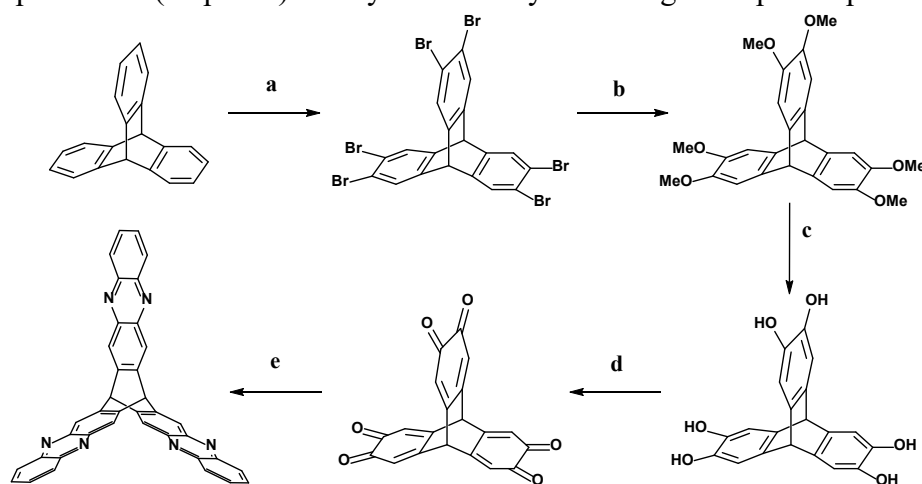
S6.3 Ex-situ ESR spectra

S6.4 Temperature dependent ESR spectra

### Reference

## S1. Preparation and Characterization of Trip-Phz/SWCNT Composites

The triptycene-phenazine (Trip-Phz) was synthesized by following the reported procedures.<sup>1</sup>



Scheme S 1 Synthetic route to Trip-Phz

Reagents and conditions are shown as follows: (a) bromine, iron, chloroform, 25°C for 1h; (b) copper(I) bromide, 25wt% sodium methoxide in methanol, ethyl acetate, toluene, 80°C for 20h; (c) boron tri-bromide, dichloromethane, 25°C for 18h; (d) 2,3-dichloro-5,6-dicyano-1,4-benzoquinone, tetrahydrofuran, 25°C for 20h; (e) o-phenylenediamine, N,N-dimethylaminopyridine, ethanol, 75°C for 48h. The crude Trip-Phz was purified by recrystallization from THF.

### S1.1 Sample preparation

The recrystallized Trip-Phz was vacuum-assisted dried before use. SWCNT was provided by TUBALL OCSiAl Corp. (99%), with SWCNT length of >5  $\mu\text{m}$ , outer mean diameter of  $1.6 \pm 0.4$  nm, containing a tiny amount of metal catalyst impurities Cr (<335 ppm), Fe (8000 ppm), Cu (<20 ppm), Ni (<350 ppm), Zn (<20 ppm). Other materials, like benzene, dimethyl formamide (DMF), triethylamine (TEA), dimethyl sulfoxide (DMSO), acetonitrile, and 4-Hydroxy-2,2,6,6-tetramethylpiperidine 1-Oxyl free radical (TEMPOL) were used without further purification.

The Trip-Phz/SWCNT composites were synthesized via sonication-induced self-assembly.<sup>2</sup> At first, a quantity of 1 to 10 mg of Trip-Phz crystalline powder, varying according to the target mass ratio, was dispersed in 2.5 ml of benzene within a 20 ml test tube by sonicating at 45W for 10 mins. Then, 5 mg of SWCNTs was added into the well-dispersed Trip-Phz suspension and the mixture was sonicated again for 30 mins to ensure homogenous mixing. This was performed using a BM EQUIPMENT Nanoruptor NR-350, operating with a cycle of 30 s of sonication followed by 60 s of rest, repeated for 120 cycles. This process aimed to de-bundle the SWCNTs and promote the formation of a hard gel. The obtained hard gel was subjected to freeze-drying under vacuum overnight to remove the solvent. Subsequently, to ensure the complete removal of any residual benzene, the freeze-dried Trip-Phz/SWCNT aerogel was dried at 60 °C for 2 h.

The final product, Trip-Phz/SWCNT aerogel, was then pressed into a thin film to serve as a binder-free electrode in solid-state electrochemical tests. The mass loading of the Trip-Phz/SWCNT composites ranged from 2 to 5  $\text{mg}/\text{cm}^2$ .

To determine the maximum amount of Trip-Phz that SWCNTs can absorb, a diluted dispersion was prepared with 0.5 mg of SWCNTs and 5 mg of Trip-Phz in 3 mL of DMF/TEA mixture. The obtained dispersion was filtered through a membrane and thoroughly washed with benzene to remove unabsorbed Trip-Phz. The final yield of 1.3 mg of Trip-Phz/SWCNT composite indicates that SWCNTs can absorb a maximum of 1.6 times their weight in Trip-Phz. This maximum absorption ratio was a target for Sample 5, which was prepared with a Trip-Phz to SWCNTs weight ratio of 10:5, reaching the upper limit of Trip-Phz absorption by the SWCNTs.

## S1.2 TEM images

For transmission electron microscopy (TEM) analysis, diluted dispersions of SWCNTs and Trip, Phz, and Trip-Phz were prepared. A typical dispersion involved sonicating 0.17mg of SWCNTs and 1.85 mg of Trip-Phz in a 2 mL DMF/TEA mixture (v/v=3/1). A well-dispersed suspension was then deposited onto a Cu mesh for TEM.

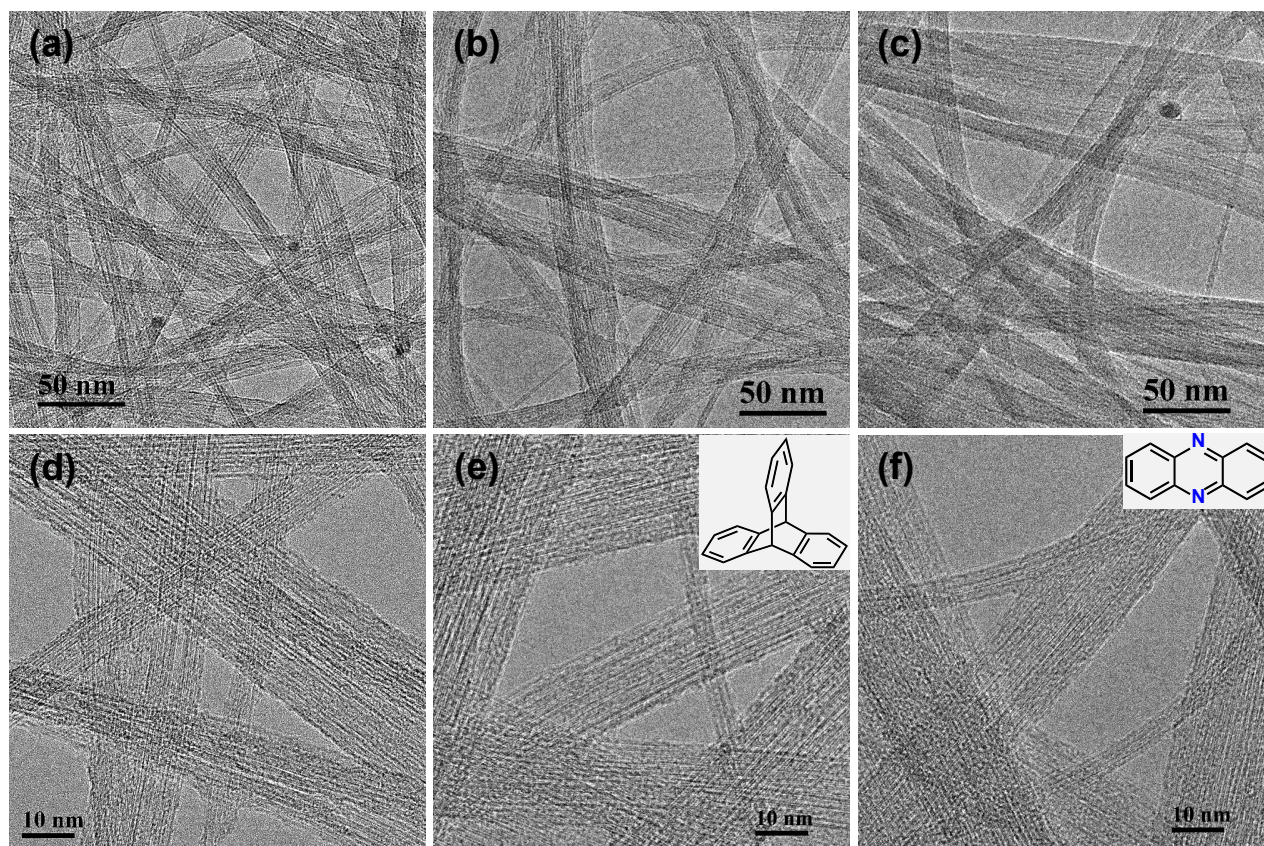


Figure S 1 TEM images of SWCNTs (a,d), Trip/SWCNT (b,e) and Phz/SWCNT (c,f) composites.

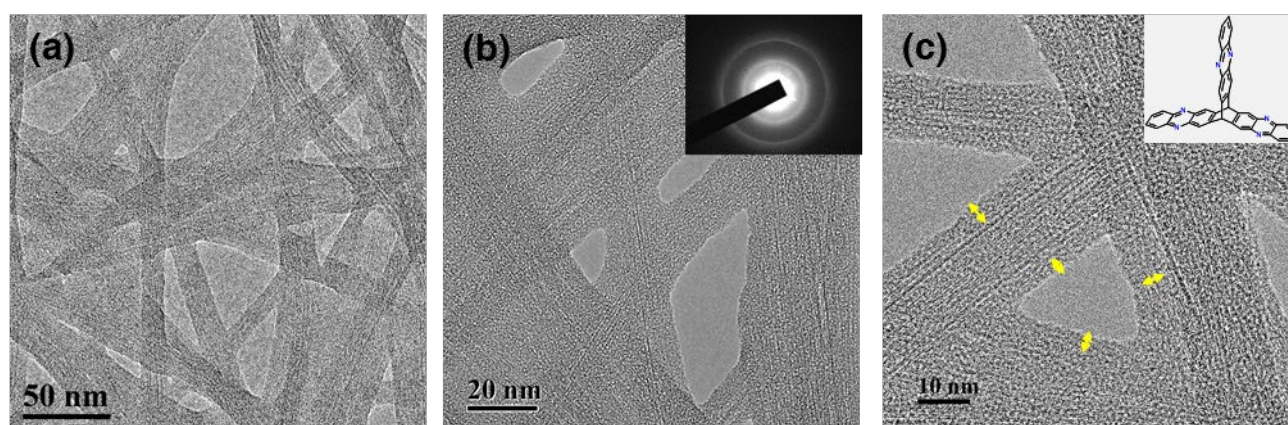


Figure S 2 TEM images of Trip-Phz/SWCNT composite. The inset of panel b illustrates the selected area diffraction pattern of composite.<sup>2</sup>

TEM images revealed the morphology of SWCNT bundles, some containing embedded metal particles. The diameter of these SWCNT bundles ranged from 5 to 10 nm. In the absence of Trip or Phz molecules in Fig. S1.1, no evidence of their absorption onto the SWCNT bundles was observed. In contrast, the presence of strong  $\pi$ - $\pi$  interaction facilitated the successful absorption of thin-layer of Trip-Phz (highlighted by yellow arrows) onto the SWCNTs. The selected area diffraction of Trip-Phz/SWCNT composite displays two Debye-Scherrer rings, which could be attributed to the 10 and 11 reflections of SWCNTs, suggesting the presence of amorphous Trip-Phz layer. Interestingly, the TEM images

also revealed a decrease in the size of the SWCNT bundles. It can be explained by the fact that the triptycene derivative can potentially de-bundle the SWCNTs.

### S1.3 FTIR

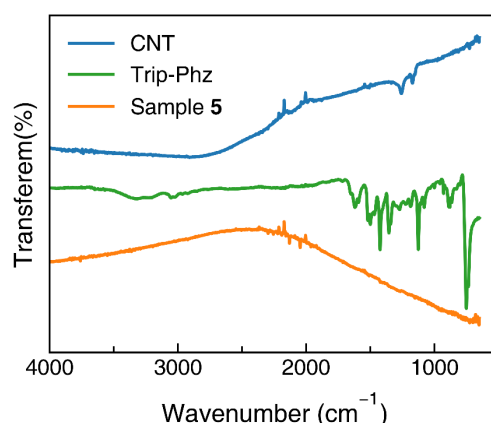


Figure S 3 FTIR of SWCNT, Trip-Phz, and Trip-Phz/SWCNT composite (Sample 5).

Fourier-transform infrared spectroscopy (FTIR) of Sample 5 shows a strong absorption edge in the near IR region, indicating the semiconductive nature of Trip-Phz/SWCNT composites.

## S2. Cyclic Voltammograms in Solution

A three-electrode setup was employed for the electrochemical characterization of the Trip-Phz in solution. A Pt rod served as the working electrode, a Pt mesh was used as the counter electrode, and a Pt wire acted as the reference electrode. A 0.1 M solution of tetrabutylammonium perchlorate (TBAP) was prepared in either DMSO or acetonitrile as the supporting electrolyte. 0.2 M acid was added to the supporting electrolyte served as the proton source. Due to the slight solubility of Trip-Phz, a saturated solution was prepared by adding enough Trip-Phz crystalline powder into the corresponding supporting electrolyte. Alternatively, CV curves of ferrocene were measured in the same supporting electrolytes, allowing for calibration of the redox potential of Trip-Phz. All CV measurements were carried out under a continuous nitrogen bubbling environment to remove the dissolved oxygen.

### S2.1 Neutral DMSO

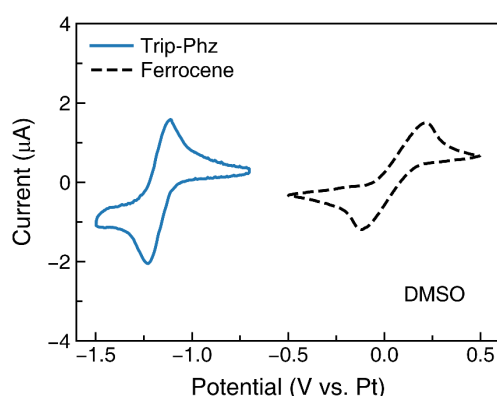


Figure S 4 Cyclic voltammograms of Trip-Phz (blue) and ferrocene (black dashed) recorded in neutral DMSO electrolyte at 50 mV/s ( $E_{Fc/Fc^+} = +0.047$  V vs. Pt).

### S2.2 Acidic DMSO

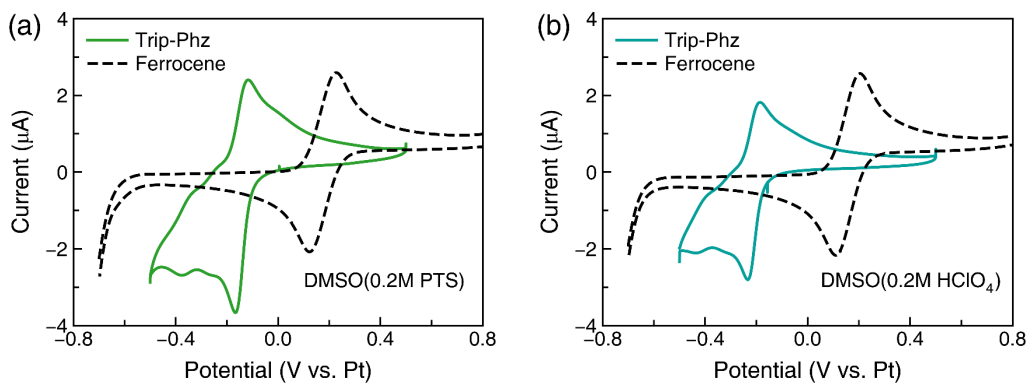


Figure S 5 (a) Cyclic voltammograms of Trip-Phz (green) and ferrocene (black dashed) recorded in 0.2 M PTS/DMSO electrolyte at 50 mV/s ( $E_{Fc/Fc^+} = +0.18$  V vs. Pt). (b) Cyclic voltammograms of Trip-Phz (teal) and ferrocene (black dashed) recorded in 0.2 M HClO<sub>4</sub>/DMSO electrolyte at 50 mV/s ( $E_{Fc/Fc^+} = +0.16$  V vs. Pt).

### S2.3 Acidic acetonitrile

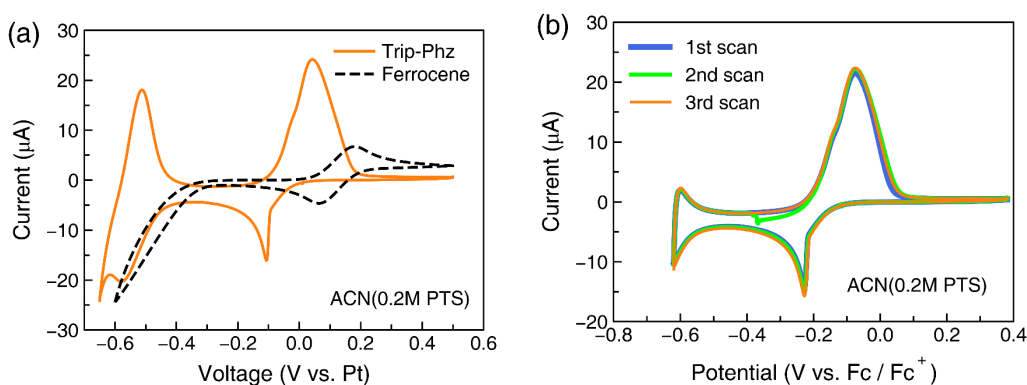


Figure S 6 (a) Cyclic voltammograms of Trip-Phz (orange) and ferrocene (black dashed) recorded in 0.2 M PTS/acetonitrile (ACN) electrolyte at 50 mV/s ( $E_{Fc/Fc^+} = +0.12$  V vs. Pt). (a) The first three cycles of cyclic voltammograms of Trip-Phz at 50 mV/s within an electrochemical window of -0.62 to 0.38 V vs. Fc/Fc<sup>+</sup>.

### S3. Solid-State Electrochemistry

Specific capacity and capacitance are crucial parameters for evaluating the electrochemical performance of battery and capacitor devices, respectively. They are related through the following equation:

$$\text{Specific Capacity [mAh/g]} = 3.6 \cdot \text{Specific Capacitance [F/g]} \cdot \Delta V[V] \quad (1)$$

Specific capacitance ( $C_{\text{cap}}$ ) can be determined from the galvanostatic charge-discharge profile using the equation:

$$\text{Specific Capacitance [F/g]} = \frac{I[A] \cdot \Delta t[s]}{\Delta V[V] \cdot m[g]} \quad (2)$$

Alternatively, specific capacitance can be calculated based on cyclic voltammetry data:

$$\text{Specific Capacitance [F/g]} = \frac{\int i[A]dt}{\Delta V[V] \cdot m[g]} = \frac{1000 \int i[A]dV}{\Delta V[V] \cdot \nu[mV/s] \cdot m[g]} \quad (3)$$

Then, the energy density can be expressed by:

$$\text{Energy Density [Wh/kg]} = \frac{C_{\text{cap}}[F/g] \cdot \Delta V^2[V^2]}{2 \cdot 3.6} \quad (4)$$

And the powder density can be determined as:

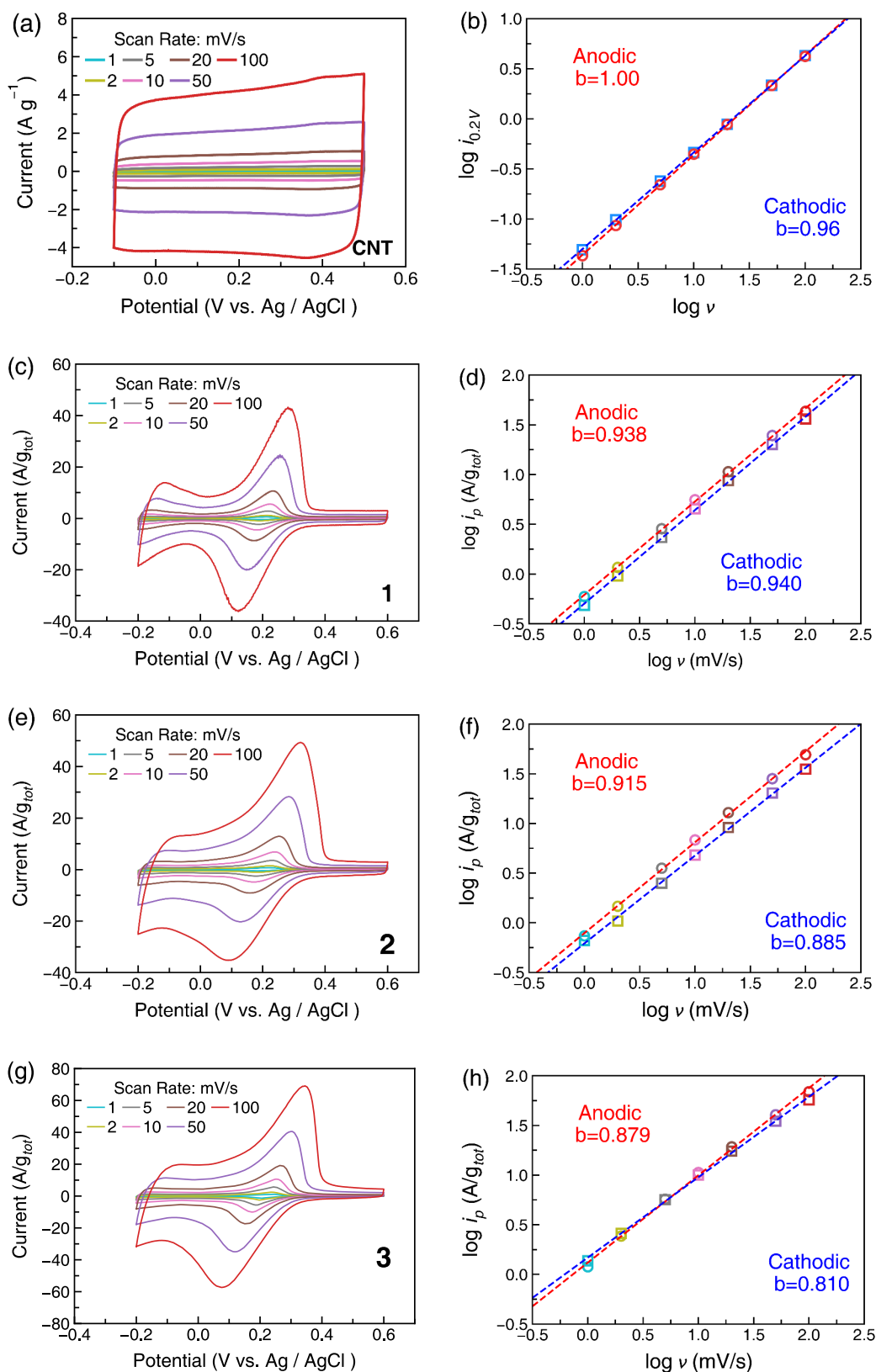
$$\text{Power Density [W/kg]} = \frac{\text{Energy Density [Wh/kg]}}{\Delta t[s]/3600} \quad (5)$$

Based on the assumed three-electron redox reaction for Trip-Phz, its theoretical can be estimated as:

$$\text{Theoretical capacity [mAh/g]} = \frac{F[C/mol] \cdot n}{3.6 \cdot M_w[g/mol]} = \frac{96485 \cdot 3}{3.6 \cdot 560} = 143.6 \quad (6)$$

In this work, solid-state electrochemical measurements were performed using a BioLogic SP-150 workstation. A 1M H<sub>2</sub>SO<sub>4</sub> aqueous solution was used as an electrolyte. The Trip-Phz/SWCNT thin film was carefully handled using a titanium tweezer, acting as the working electrode. A Pt wire served as the counter electrode, and an Ag/AgCl electrode (195mV vs. RHE, RE-1B ALS Co.) was used as the reference electrode. Nitrogen gas continuously bubbled during the measurement.

### S3.1 Ratio dependent CV curves





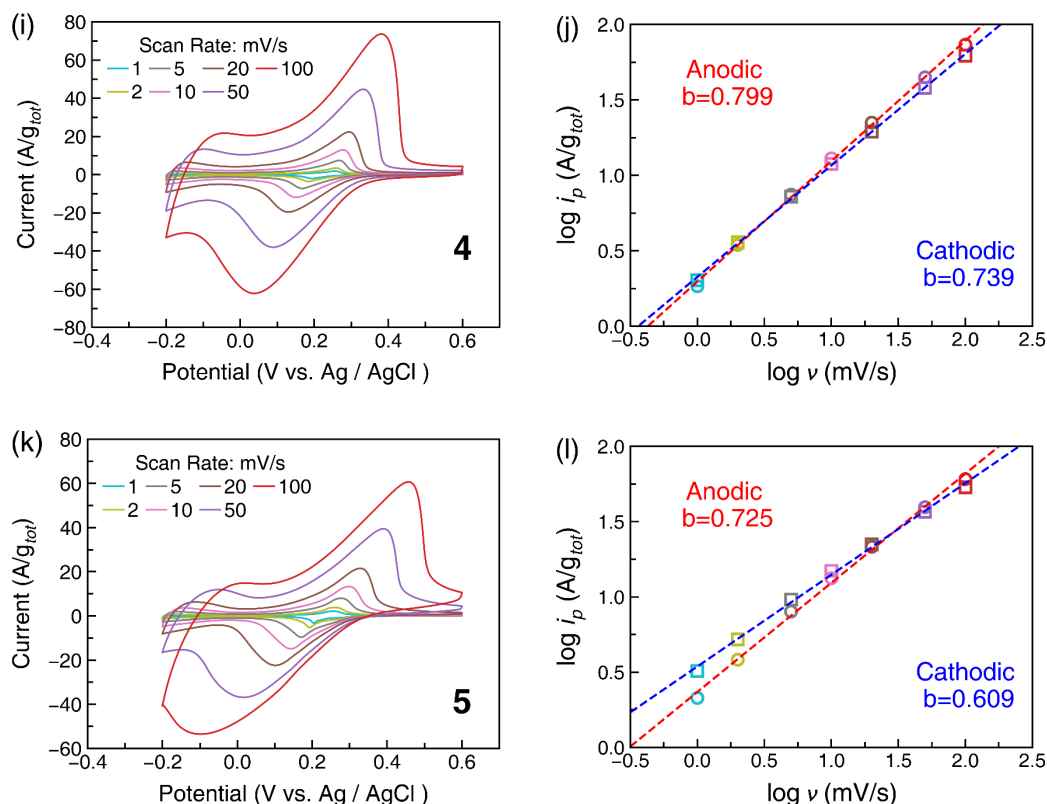


Figure S 7 Cyclic voltammograms (CVs) of the bare SWCNT (a) and Trip-Phz/SWCNT composites (1: c, 2: e, 3: g, 4: i, 5: k) at various scan rates (1-100 mV/s). The corresponding log-log plots of peak current ( $i_p$ ) vs. scan rate ( $\nu$ ) for SWCNT (b) and Trip-Phz/SWCNT composites (1: d, 2: f, 3: h, 4: j, 5: l).

The peak currents in CV curves follow a power law with the scan rate expressed as,  $i_p = a\nu^b$ . Exponent  $b$  reflects the mechanism of the charge storage process at the electrode. It can be determined by fitting a straight line to the log-log plot of peak current vs. scan rate. The obtained values of  $b$  for both the cathodic and anodic scans are presented in Figure S3.1.

Scan Rate (mV/s)	1	2	5	10	20	50	100	
CNT	41.3	40.7	41.5	40.9	38.8	37.5	36.7	
1	Total	130.8	133.7	133.2	131.1	131.1	127.9	124.4
	Trip-Phz	578.1	598.8	591.5	582.0	592.2	579.8	563.1
2	Total	194.1	198.2	194.6	190.9	185.6	176.3	165.8
	Trip-Phz	503.9	515.0	505.0	495.3	481.9	457.8	429.8
3	Total	281.6	284.5	277.7	270.2	261.6	245.6	228.4
	Trip-Phz	521.8	528.4	513.9	499.4	484.4	453.7	420.2
4	Total	344.5	339.4	326.0	314.2	301.4	279.8	259.2
	Trip-Phz	561.1	552.8	529.2	509.3	488.9	452.9	418.2
5	Total	384.6	375.5	359.8	342.0	317.2	274.9	215.1
	Trip-Phz	556.2	542.8	519.0	492.6	456.3	393.6	304.3

Table S 1 Specific capacitance of Trip-Phz/SWCNT composites.

The specific capacitances of each sample at various scan rates were calculated using equation (3) normalized by total electrode weight or Trip-Phz weight only. In the latter case, the contribution of Trip-Phz to the capacitance by subtracting the inherent capacitance of SWCNTs, which was estimated by the capacitance of a base SWCNT electrode.

### S3.2 Three component contributions

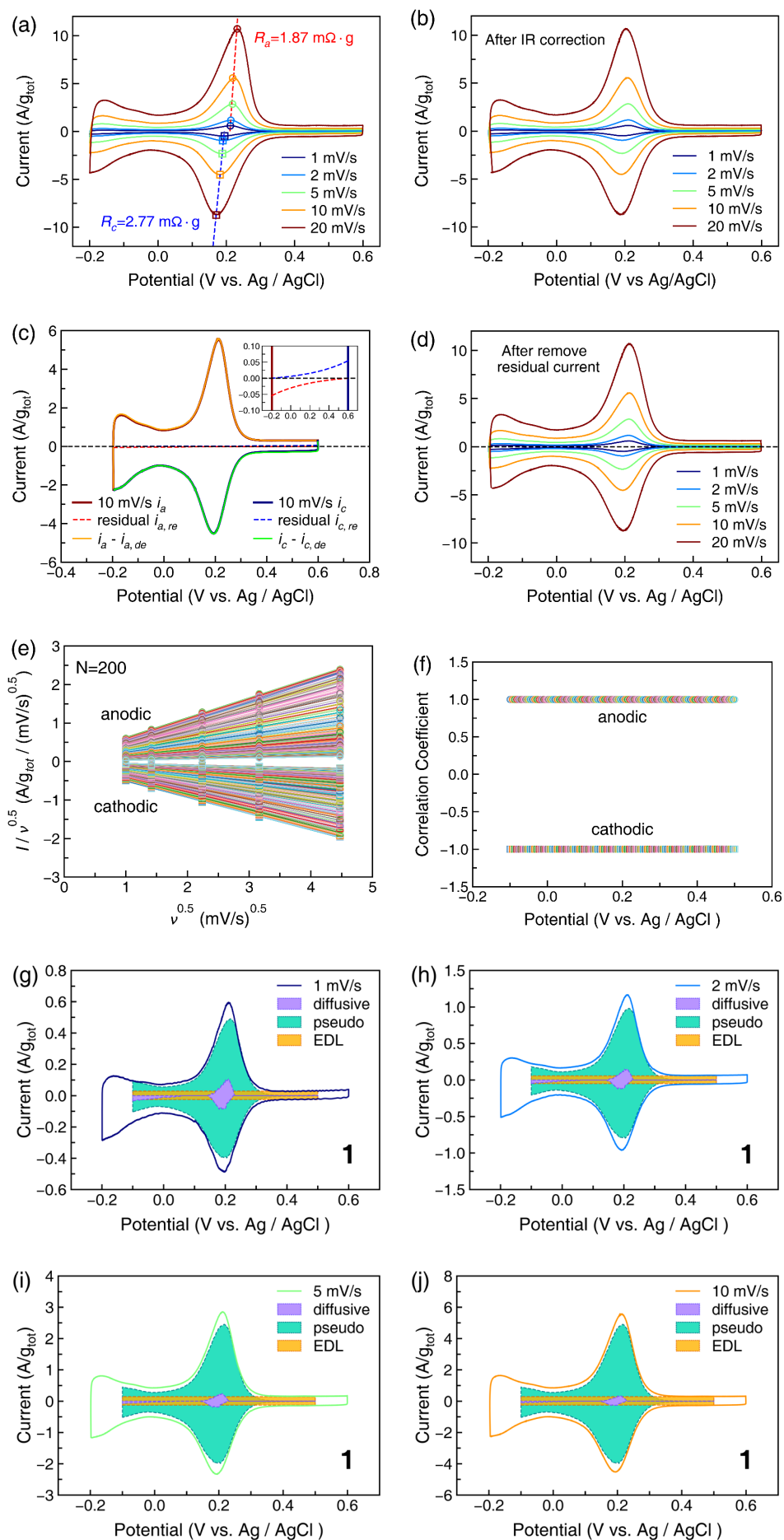


Figure S 8 IR correction (a-b), de-residual (c-d), linear fitting (e-f) of CV curves at scan rates of 1-20 mV/s for Sampl 1. The decomposition of CV curves (g-j) at scan rates of 1-10 mV/s for Sampl 1.

As described in the main text, the equation  $(i - i_{dl})/v^{0.5} = k_1 v^{0.5} + k_2$  allows the separation of contributions from the electric double layer  $i_{dl}$ , pseudo-capacitance  $i_{ps}$ , and diffusion  $i_{diff}$  through linear fitting of  $(i - i_{dl})/v^{0.5}$  vs.  $v^{0.5}$ . However, errors arise due to Ohmic polarization and residual current. The Ohmic polarization was introduced from the measurement circuit, causing the potential of current's peak ( $V_p$ ) to shift with increasing scan rate (negative/positive for cathodic/anodic scans), as shown in Fig. S8a. The residual current ( $i_{a, re}$  for the anodic scan and  $i_{c, re}$  for the cathodic scan) emerges when reversing the scan direction.

To compensate for Ohmic losses, the parasitic resistance ( $R$ ) is estimated through linear fitting of  $V_p$  and  $i_p$  in Fig. S8a:  $R = V_p / (i_p - \text{Constant})$ . This resistance is then used for IR compensation:  $V'(i) = V(i) - iR$ . The residual currents are expressed by the equations:  $i_{a, re} = 1 - \text{Exp}[(V - c)/d]$ ;  $i_{c, re} = \text{Exp}[(V - a)/b] - 1$ .<sup>3</sup> The constants (a-d) can be determined by boundary conditions:  $i_{c, re}(V_{min}) = 0$ ;  $i_{c, re}(V_{max}) = i_{ps}(V_{max}) + i_{diff}(V_{max})$ ;  $i_{a, re}(V_{max}) = 0$ ;  $i_{a, re}(V_{min}) = i_{ps}(V_{min}) + i_{diff}(V_{min})$ . The CV current is then calibrated as:  $i' = i - i_{de}$  (refer to Fig. S8c). For clarity, the calibrated  $i'$  and  $V'$  are rewritten as  $i$  and  $V$  (Fig. S8d).

The calibrated CV curves are divided into 200 segments. Linear fitting within each segment allows the estimation of coefficients  $k_1$  and  $k_2$ . The correlation coefficient for each fit is presented in Fig. S8f. Similar quantitative analyses were performed on Samples 2-5.

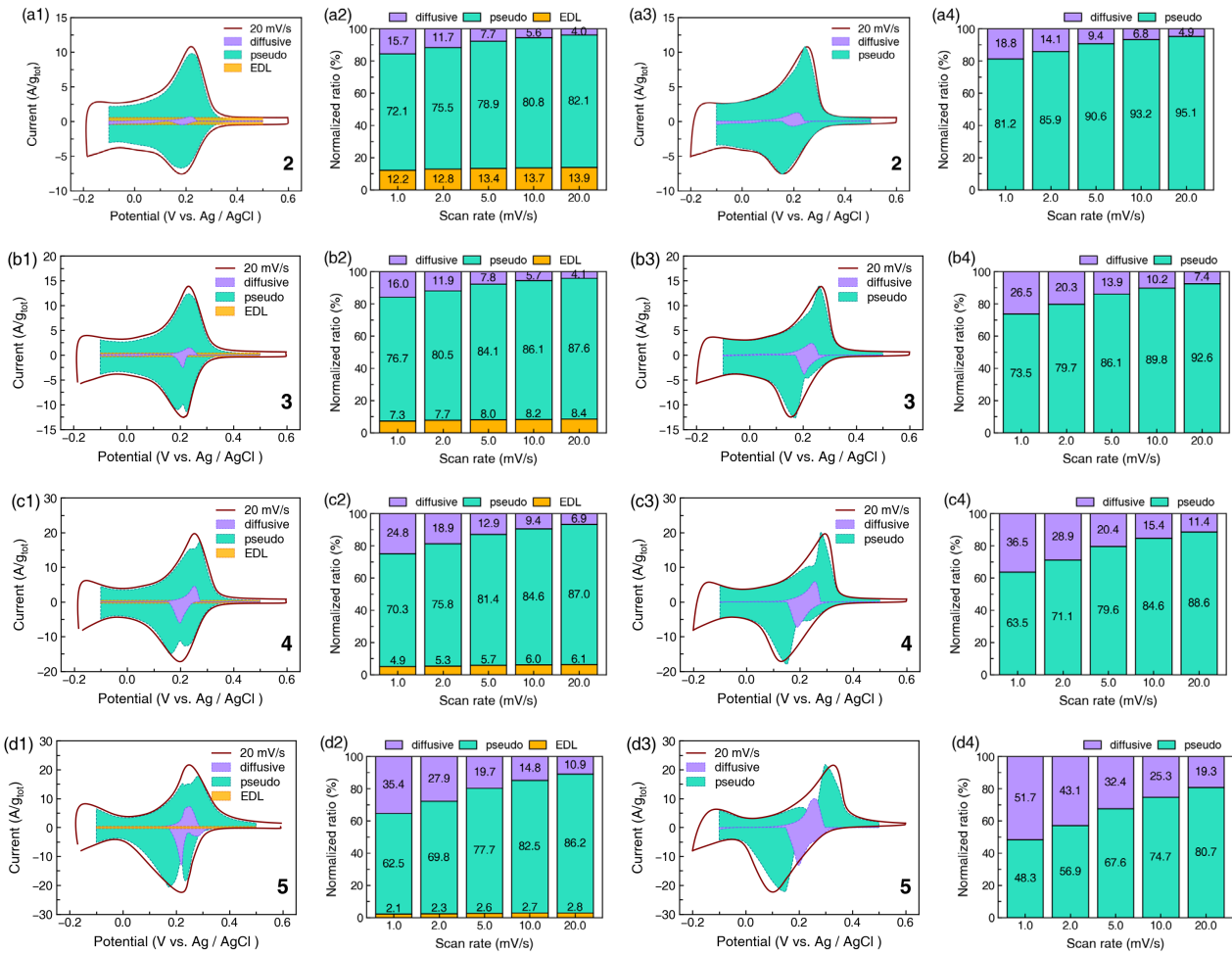


Figure S9 Decomposition of compensated CV curve into three components – diffusive, pseudo-capacitive, electric double-layer capacitive currents (a1-d1) and the corresponding normalized ratios (a2-d2) for Samples 2-5. Decomposition of original CV curve into two components – diffusive, pseudo-capacitive currents (a3-d3) and the corresponding normalized ratios (a4-d4).

In many cases, the original CV curves of Samples 2-5 were also analyzed by separating them into two components. This was achieved through direct linear fitting of  $i/v^{0.5}$  vs.  $v^{0.5}$  across 200 potential points. In this process, the contribution of electric double-layer was integrated into the pseudo-capacitive component. In regions with low Trip-Phz content (Sample 2), the normalized ratios of diffusive and

pseudo-capacitive components (a4) derived from the original CV curve in agreement with those (a2) obtained from the compensated CV curve. However, for Sample 5, the presence of significant Ohmic polarization led to a notable shift in the peak potential of CV curves. This resulted in an overestimation of the contribution of the diffusive component.

### S3.3 Electrochemical impedance spectroscopy

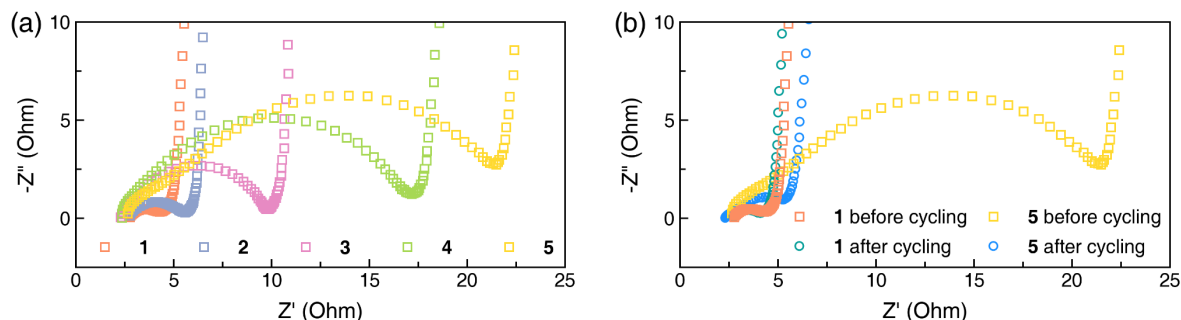
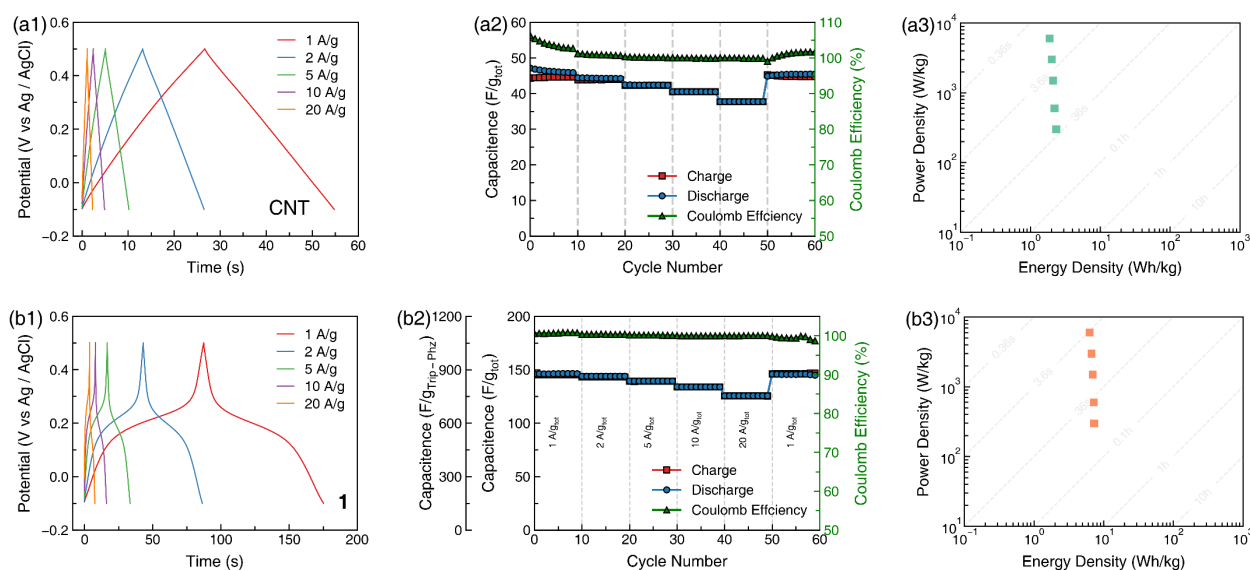


Figure S 10 (a) Electrochemical impedance spectroscopy (EIS) of as-prepared Trip-Phz/SWCNT composites. (b) EIS of pristine and cycled Sample 1 and 5.

The EIS measurements were conducted using a BioLogic SP-150 workstation with an AC voltage of 5 mV amplitude across a frequency range from 500 kHz to 1 Hz. All samples exhibited a similar solution resistance ( $R_s \sim 2.5$  Ohm), observed as the high-frequency intercept on the x-axis, indicating minimal electrolyte conductivity. Furthermore, all samples displayed a small charge transfer resistance ( $R_{ct}$ ), represented by the diameter of the semicircles in the mid-frequency region, indicating rapid kinetics of charge transfer. A consistent decreasing trend in  $R_{ct}$  was observed with decreasing Trip-Phz content (from Sample 5 to Sample 1), which is consistent with the enhanced rate performance observed in Fig. S10 and Fig. 3 for samples with lower Trip-Phz content. Interestingly, all samples demonstrated a further decrease in  $R_c$  after undergoing charge-discharge cycles. This improvement was particularly significant for Sample 5, where  $R_{ct}$  dropped from 19 to 3.1 Ohm. Two possible explanations were proposed for this decrease in  $R_{ct}$ . On the one hand, protonation of Trip-Phz during cycling might facilitate faster ion transport and charge transfer. On the other hand, the cycling process could induce rearrangement of Trip-Phz molecules, potentially resulting in stronger  $\pi$ - $\pi$  interactions among them.

### S3.4 Charge-discharge profiles



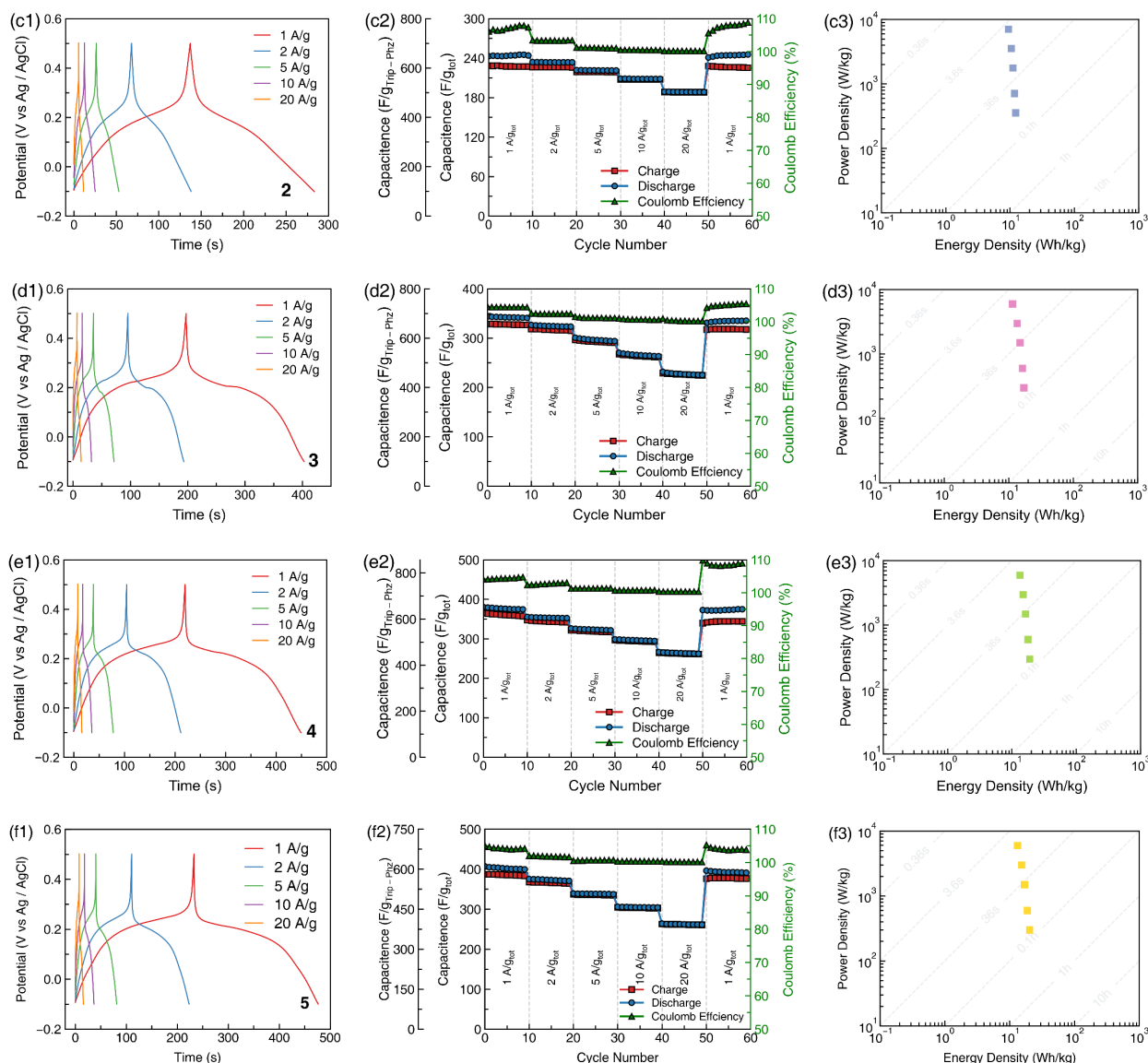


Figure S 11 Electrochemical performance of SWCNT and Trip-Phz/SWCNT composites. (a1-f1) Charge-discharge profiles of SWCNT and Samples **1-5** at various current densities 1-20 A/g. (a2-f2) Specific capacitance and Coulomb efficiency of SWCNT and Samples **1-5**, each current density run 10 cycles. (a2-f3) Ragone plot for SWCNT and Samples **1-5** supercapacitors.

The specific capacitance exhibits a decrease as the Trip-Phz content in the composite increases. This trend is more obvious in the lower current density. At higher current densities, the process becomes limited by diffusion. This means that the transport of protons towards the inner layers of the thicker Trip-Phz layer (for the sample with higher Trip-Phz content) becomes restricted. This limitation hinders the effective utilization of the entire Trip-Phz in composite, leading to a more significant reduction in capacitance for Sample **5** compared to samples with lower Trip-Phz content. The discharge capacitance is slightly higher than the charge capacitance, which is attributable to the instability of reduced Trip-Phz radical cation. During the discharge process, the reduced form of Trip-Phz might undergo a disproportionated reaction, leading to a higher discharge capacity compared to the charge capacity.

## S4. DFT Calculation

As implemented in VASP v.6.3.0 code,<sup>4,5</sup> we performed density functional theory (DFT) calculations based on the plane-wave based projector augmented wave (PAW) method<sup>6</sup> to obtain optimized structures for Trip-Phz on a carbon nanotube. In our DFT calculations, we used the generalized gradient approximation (GGA) with the functional by Perdew-Burke-Ernzerhof (PBE)<sup>7</sup>. Long-range interactions between Trip-Phz and a carbon nanotube are expected to stabilize the hybrid structures, and thus we added empirical dispersion correction to PBE functional (PBE-D3 method), developed by Grimme et al.<sup>8</sup> To describe the Trip-Phz/SWCNT system, we constructed a hexagonal lattice where a SWCNT attached by a Trip-Phz is located at the center. Separations of SWCNTs located on adjacent cells are 20 Å, which are large enough to avoid inter-tube interactions. The length of the tube in a cell is about 17 Å which is also large enough to avoid interactions between Trip-Phz molecules located on adjacent cells. In the supercell calculations, the Brillouin zone sampling was restricted to only the  $\Gamma$  point. For the plane-wave basis set, a cutoff energy of 500 eV was used. In the optimizations, we judged that the optimizations are converged when the maximum forces on all atoms are less than 0.03 eV/Å.

### S4.1 Interatomic separation

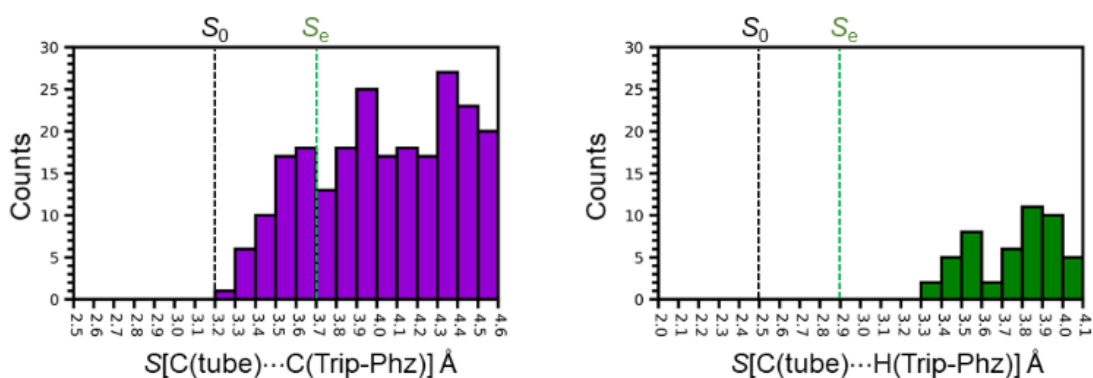


Figure S 12 Histograms of interatomic separations between Tri-Phz and SWCNT in the optimized structure for Trip-Phz/(21,0) tube. (a) carbon separations between Trip-Phz and SWCNT, associated with  $\pi$ - $\pi$  interactions, and (b) separations between an H atom of Trip-Phz and a carbon atom of SWCNT, associated with CH- $\pi$  interactions. The smallest limit of internuclear separation between benzene and naphthalene without any  $\pi$ - $\pi$  or CH- $\pi$  repulsive interactions ( $S_0$ ), as well as the equilibrium separations ( $S_e$ ), reported in our previous study<sup>9</sup>, are given by dotted lines.

### S4.2 Stabilization energy

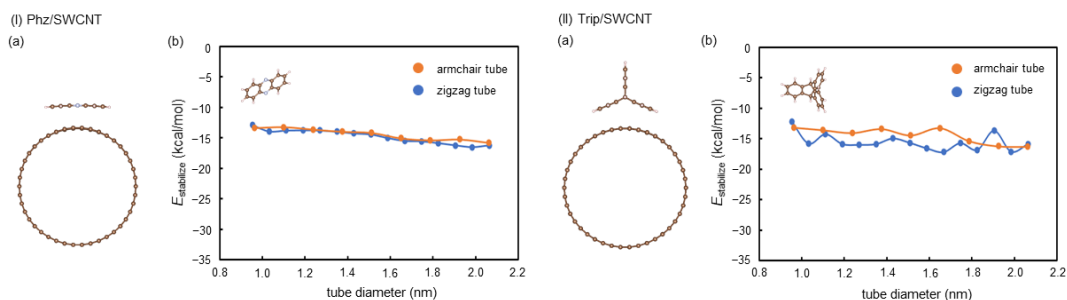


Figure S 13 Structural and energetic features of (I) Phz/SWCNT and (II) Trip/SWCNT. (a) A representative optimized structure for Phz or Trip on SWCNT (Phz/(21,0) tube or Trip/(21,0) tube). (b) Changes of  $E_{\text{stabilize}}$  values as a function of the tube diameter. Negative  $E_{\text{stabilize}}$  values indicate that Phz/SWCNT and Trip/SWCNT composites are energetically stable relative to the dissociation limit toward a corresponding molecule and SWCNT.

## S5. Physical Properties

### S5.1 Electrical conductivity

A four-probe method was employed to measure the electrical conductivity of SWCNT/Trip-Phz thin films. Gold wires and gold paste contacts were utilized to connect the films to the measurement device. A Quantum Design PPMS system varied the temperature from 5 to 300 K for the temperature dependence measurements. Pristine samples (as-prepared Samples **1** and **5**) were electrochemically reduced by discharging them to  $-0.1$  V. Specifically, the SWCNT/Trip-Phz thin films were cycled by applying current through the gold wires. Then, the reduced samples were washed and dried before the second conductivity measurements.

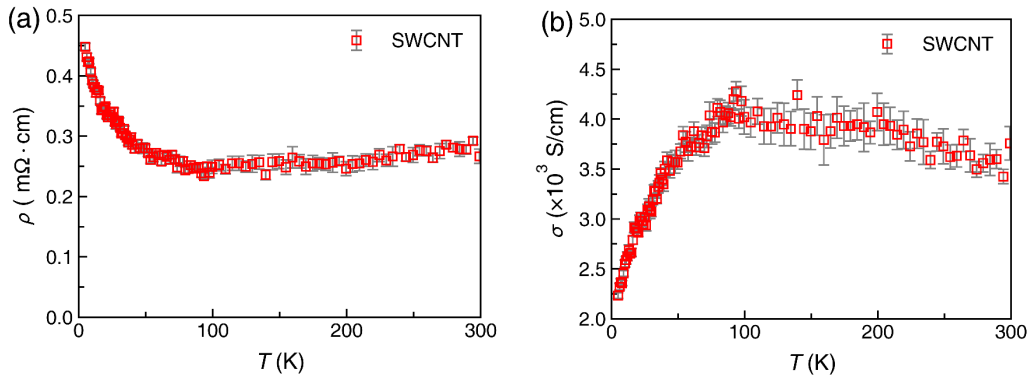


Figure S 14 Temperature dependence of the electrical conductivity of SWCNT thin film. Sample size: width=0.165 cm, thickness=30  $\mu\text{m}$ , length=0.082 cm.

SWCNT film exhibits metallic behavior within the temperature range of 100 to 300 K. However, upon cooling below 100 K, the SWCNT film's resistivity increased, which can be attributed to the presence of semiconductive SWCNTs within the metallic SWCNT matrix.

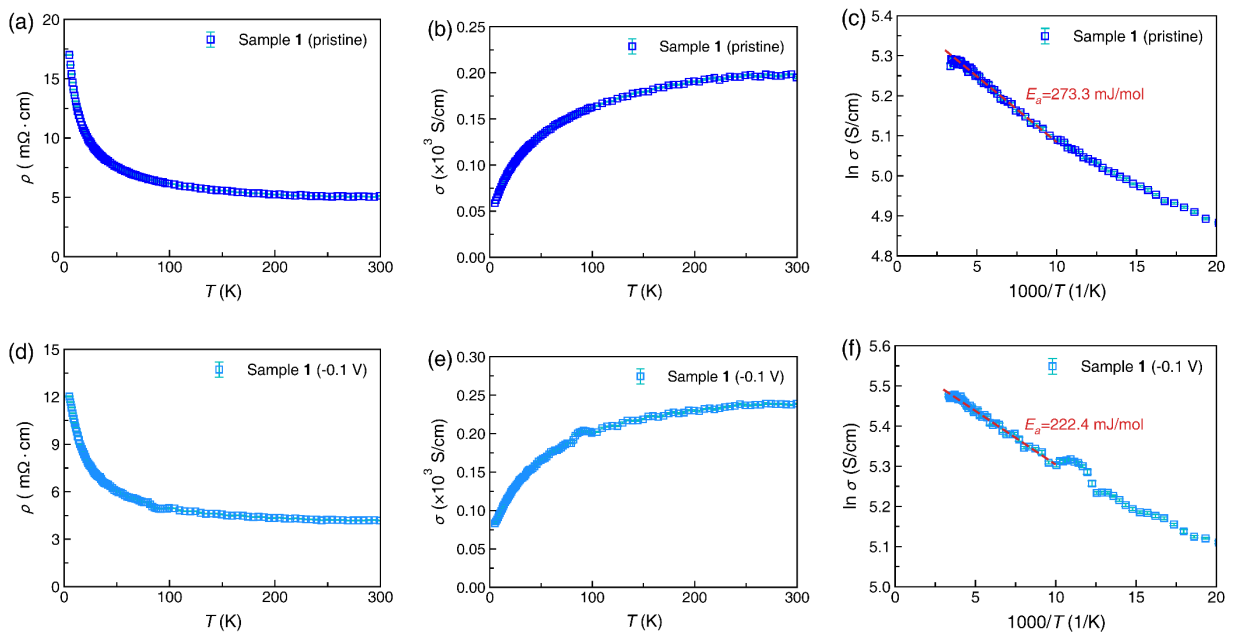


Figure S 15 Temperature dependence of the electrical conductivity of pristine Sample **1** (a-c) and discharged Sample **1** (d-f). Sample size: width=0.170 cm, thickness=75  $\mu\text{m}$ , length=0.080 cm.

Sample 1 exhibits semiconductive behavior across the measured temperature range. Notably, its room-temperature conductivity ( $\sigma_{RT}$ ) slightly increased after reduction to  $-0.1$  V. This improvement likely stems from enhanced  $\pi$ - $\pi$  interactions between the SWCNTs and reduced Trip-Phz molecules. Stronger  $\pi$ - $\pi$  interactions act like bridges, facilitating the hopping of charge carriers between SWCNT bundles. Consequently, the activation energy ( $E_a$ ) required for charge transport within the composite material decreases.

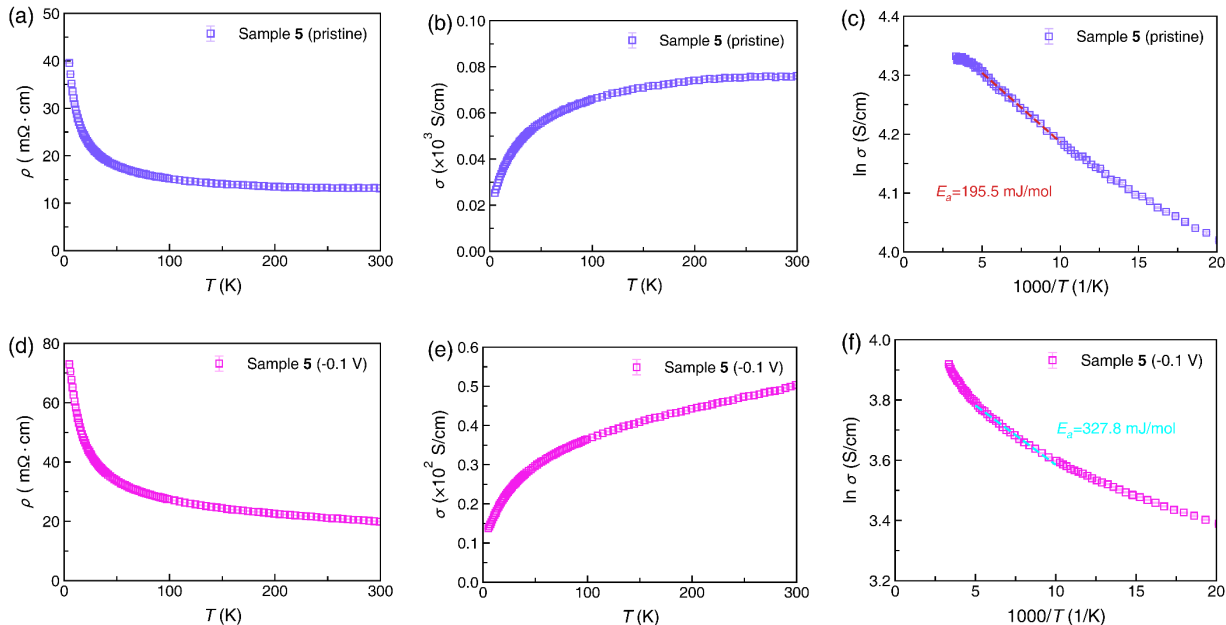


Figure S 16 Temperature dependence of the electrical conductivity of pristine Sample 5 (a-c) and discharged Sample 5 (d-f). Sample size: width=0.150 cm, thickness=85  $\mu$ m, length=0.045 cm.

Sample 5 also exhibits semiconductive behavior, but its overall conductivity is lower due to a thicker Trip-Phz layer. In its pristine state, the activation energy of Sample 5 is comparable to that of Sample 1. However, a significant increase (1.5-fold) in  $E_a$  is observed after reduction to  $-0.1$  V. This rise suggests a larger barrier to charge transport, likely attributable to weakened  $\pi$ - $\pi$  interactions between the outer layer of Trip-Phz molecules and the SWCNTs.

Sample	$\sigma_{RT}$ (S/cm)	$E_a$ (mJ/mol)	Skin depth $\delta$ ( $\mu$ m) at 9 GHz
SWCNT	3758		8.7
1 (pristine)	195	273.3	38
1 ( $-0.1$ V)	239	222.4	34
5 (pristine)	76	195.5	61
5 ( $-0.1$ V)	50	327.8	75

Table S 2 Room-temperature conductivity, activation energy, and skin depth of SWCNT, pristine/reduced Sample 1 and 5.



## S5.2 Magnetic susceptibility

Samples were placed in plastic sample tubes for magnetic measurement. A Quantum Design MPMS (SQUID XL-5) system was used to conduct temperature-dependent susceptibility measurement within a range of 2 to 300 K. A diamagnetic correction of  $3.23 \times 10^{-4}$  emu/mol (based on the molar weight of Trip-Phz) was applied to raw data of Sample 5.

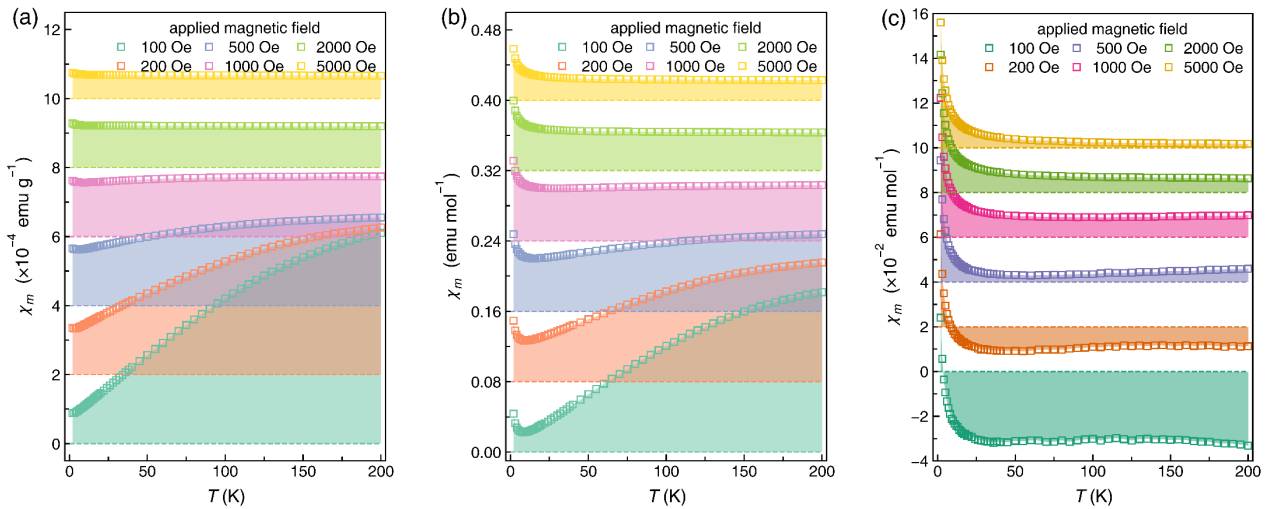


Figure S 17 Magnetic field dependence of magnetic susceptibility of SWCNT (a), Sample 5 after discharge to  $-0.1$  V (b), and the isolated contribution of Trip-Phz in Sample 5 (c). The measurements were performed using the Zero-field cooling (ZFC) mode. To isolate the Trip-Phz contribution (c), the magnetic susceptibility of SWCNT (a) was subtracted from the total susceptibility of Sample 5 (b).

The SWCNT (a) exhibits a hybrid behavior, characterized by a combination of trace-level ferromagnetism and intrinsic antiferromagnetism.<sup>10</sup> In contrast, Sample 5 ( $-0.1$  V, b) displays an additional paramagnetic component compared to SWCNT, which is attributed to the presence of electrochemically induced radicals. Assuming the magnetic susceptibility of SWCNT remains unchanged before and after electrochemical cycling, the contribution of Trip-Phz radicals to the overall susceptibility can be isolated and demonstrated in Fig. S4.4c.

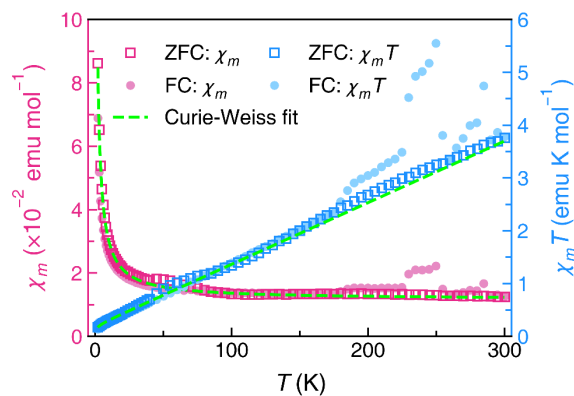


Figure S 18 Temperature dependent magnetic susceptibility of Trip-Phz radicals, measured under both zero-field cooled (ZFC) and field-cooled (FC) conditions with an applied magnetic field of 1 kOe. The right axis displays the products of susceptibility and temperature plotted against the temperature.

The isolated magnetic susceptibility of Trip-Phz radicals follows the modified Curie-Weiss law,  $\chi_m = C_m/(T - \theta) + \chi_0$ . A fit based on this equation yields a Curie constant  $C_m$  of 0.199 emu K/mol, a Weiss temperature  $\theta$  of -0.72 K, a temperature independent component  $\chi_0$  of  $1.17 \times 10^{-2}$  emu/mol. The obtained Curie constant of 0.199 emu K/mol corresponds to a radical concentration of 53%, assuming the Curie constant of Trip-PhzH<sub>6</sub><sup>3+</sup> is 0.375 emu K/mol.

## S5. Electron Spin Resonance

ESR spectra were acquired using an X-band JEOL JES-FA200 spectrometer, equipped with a liquid He variable temperature controller (variable temperature range: 5 K to RT). The magnetic field of the ESR spectra was accurately calibrated using a well-defined  $Mn^{2+}$  standards. All ESR spectra were normalized by modulation width, amplitude (gain), sample weight, and the square root of microwave power. A constant modulation frequency of 100 kHz and a time constant of 0.03 seconds were used for all measurements. To quantify the number of spins within the Trip-PHz/SWCNT composites, a radical standard, 4-hydroxy-2,2,6,6-tetramethylpiperidin-1-oxyl (TEMPO), was used. TEMPO was grounded together with KBr to allow using a small amount of TEMPO as the reference in cases where the radical density of the sample is low.

The electrochemical cycled Trip-Phz/SWCNT composites were quickly rinsed with degassed water to remove any residual electrolyte. After washing, the composites were transferred to an ESR sample tube. The sample tube was then purged with nitrogen gas, preventing the cycled samples from oxidation during the ESR measurement.

### S5.1 ESR lineshape analysis

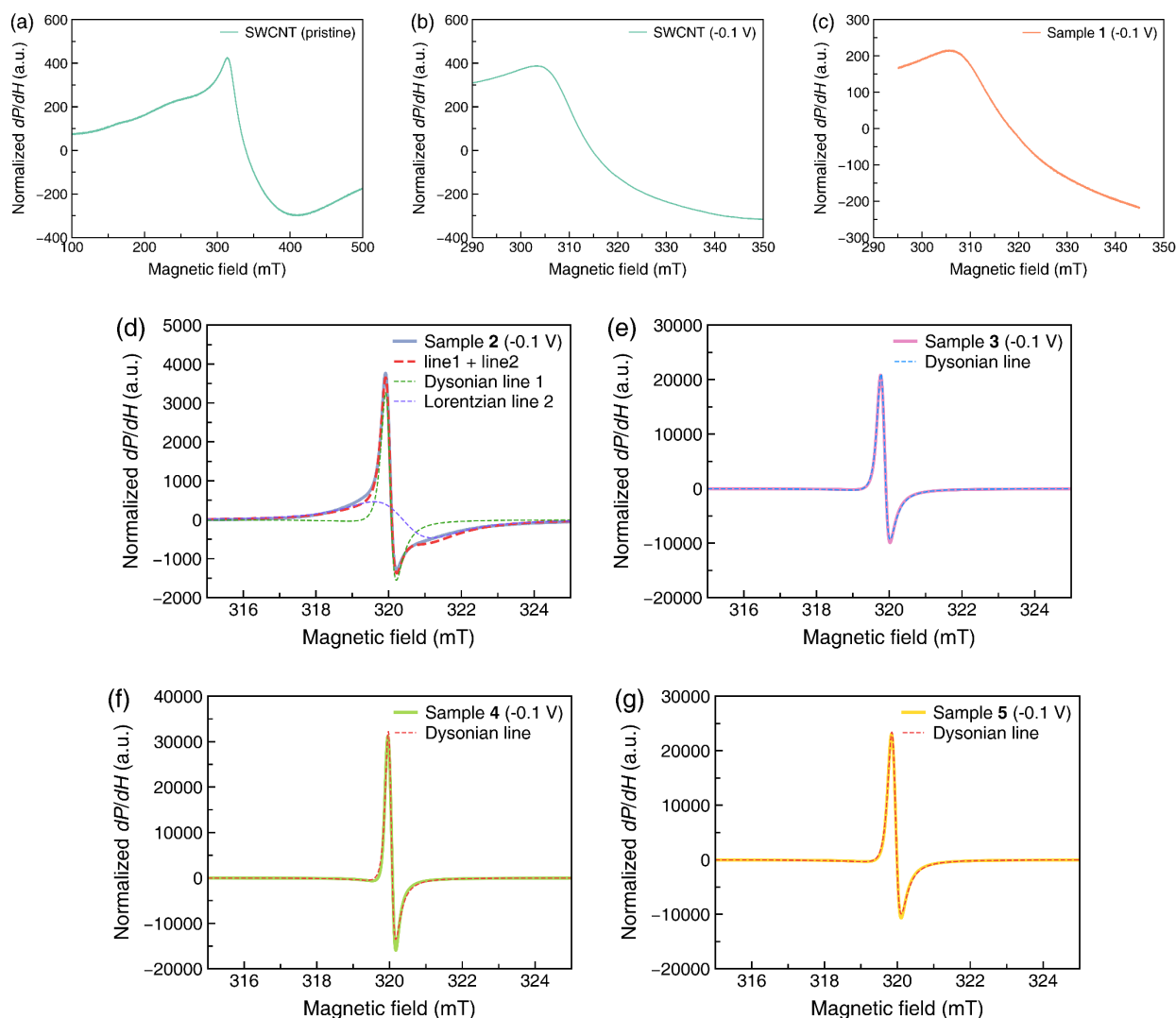


Figure S 19 ESR spectra of pristine SWCNT (a), SWCNT (b) and Sample 1 (c) discharged to  $-0.1$  V. (d-g) ESR lineshape analysis of radical signal for Samples 2-5 discharged to  $-0.1$  V.

No radical species were detected in the ESR spectra of pristine SWCNT and its discharged state. This implies that the SWCNT doesn't contain unpaired electrons. The embedded metal catalysts even in a trace level exhibited a broad ESR signal, and this signal remains unchanged even after discharging to

−0.1V. Sample 1 displayed no distinct radical signal in the ESR spectra. The observed spectrum closely resembled that of pristine SWCNTs, suggesting an absence of radicals even the Trip-Phz was reduced to the Trip-PhzH<sub>6</sub><sup>3+</sup>. Significant radical signals were identified in Samples **2-5**, indicating the presence of Trip-Phz radical cation, Trip-PhzH<sub>6</sub><sup>3+</sup>. The asymmetric ESR spectra obtained for Samples **2-5** were fitted using a Dysonian function, which incorporates both the absorption and dispersion components of signal.

$$\begin{aligned} \frac{dP}{dH} &= \frac{d}{dH} \left( \frac{\Delta H_{pp} + \alpha(H - H_r)}{(H - H_r)^2 + \Delta H_{pp}^2} + \frac{\Delta H_{pp} + \alpha(H + H_r)}{(H + H_r)^2 + \Delta H_{pp}^2} \right) \\ &= \frac{\alpha \Delta H_{pp}^2 - \alpha(H - H_r)^2 - 2\Delta H_{pp}(H - H_r)}{((H - H_r)^2 + \Delta H_{pp}^2)^2} \\ &\quad + \frac{\alpha \Delta H_{pp}^2 - \alpha(H + H_r)^2 - 2\Delta H_{pp}(H + H_r)}{((H + H_r)^2 + \Delta H_{pp}^2)^2} \end{aligned} \quad (7)$$

where  $\alpha$  reflects the dispersion-to-absorption ratio,  $H_r$  represents the resonance magnetic field, and  $\Delta H_{pp}$  donates peak-to-peak linewidth. For the symmetric ESR spectra, a Lorentzian function was used for fitting.

$$\frac{dP}{dH} = - \frac{\Delta H_{pp}^3 (H - H_r)}{\left[ \frac{3}{4} \Delta H_{pp}^2 + (H - H_r)^2 \right]^2} \quad (8)$$

Sample	Lineshape	$H_r$ (mT)	$\Delta H_{pp}$ (mT)	$\alpha$	$g$ -factor	Double Integral	Molar weight ( $\mu$ mol)
<b>2</b>	Dysonian	320.0	0.24	0.73	2.0023	5188	0.76
	Lorentzian	320.4	1.59		1.9998		
<b>3</b>	Dysonian	319.8	0.20	0.82	2.0025	6330	1.23
<b>4</b>	Dysonian	320.0	0.16	0.90	2.0024	4731	1.16
<b>5</b>	Dysonian	319.9	0.21	0.88	2.0026	7751	2.28
<b>5</b> (thin film)	Lorentzian	319.6	0.26		2.0031	456	below the lower limit
	Dysonian	319.6	0.22	0.09	2.0031		

Table S 3 The fitting results of ESR lineshape analysis for Samples **2-5** discharged to −0.1 V.

Sample **2** displays a superposition of a narrow Dysonian line and a broad Lorentzian, corresponding to the isolated localized spins and localized spins with dipole-dipole interaction. Samples **3-5** solely exhibit a narrow Dysonian line indicating the presence of isolated localized spins only. This suggests a weaker interaction between the radical centers in these samples compared to Sample **2**, probably due to the lower spin concentrations in those samples.

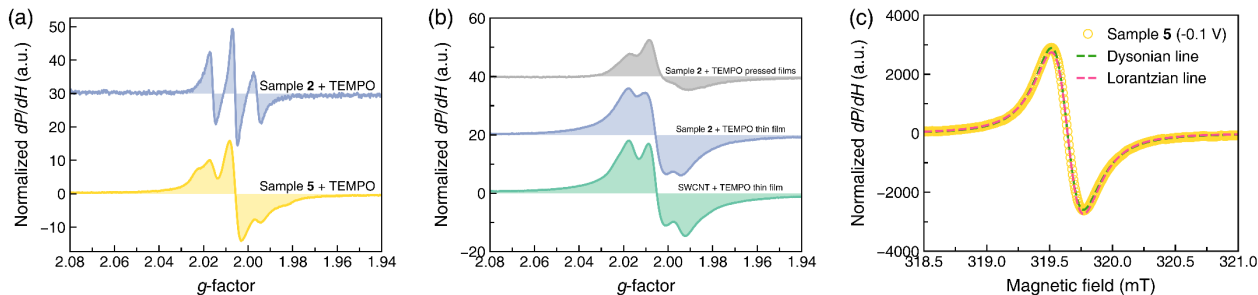


Figure S 20 (a) ESR spectra of Samples **2** and **5** with small amount of TEMPO standard. (b) ESR spectra of SWCNT and Sample **2** mixed with high TEMPO standard. (c) ESR spectrum of Sample **5** (thin film) discharged to  $-0.1$  V.

To simulate the potential interaction between SWCNT and organic radicals, Trip-Phz/SWCNT composites were co-mixed with a radical standard TEMPO. The preparation process involved the following steps: (1) A solution of TEMPO was prepared by dissolving either 0.5mg (Fig. S20a) or 4 mg (Fig. S20b) in 4 ml of benzene. (2) 1 mg of freeze-dried Trip-Phz/SWCNT composite was added into the TEMPO solution, followed by sonication for 30 minutes. (3) The Trip-Phz/SWCNT + TEMPO suspension was then filtered through a PTFE membrane (47mm diameter) and further washed with a large amount of benzene to remove unabsorbed TEMPO. (4) The Trip-Phz/SWCNT + TEMPO thin film (buckypaper) was dried and could be exfoliated on the membrane, with a thickness of  $\sim 10$   $\mu\text{m}$ .

Figure S20a depicts the hyperfine splitting of TEMPO radical with an anisotropic g-factor. The ESR spectrum of Sample **2** + TEMPO suggests rapid tumbling of the TEMPO molecules. In contrast, Sample **5** + TEMPO exhibits an ESR spectrum with restricted tumbling, suggesting a potentially stronger interaction between TEMPO and the Trip-Phz molecule. As the content of TEMPO increases (Figure S20b), the corresponding radical signal broadens due to the dipole-dipole interactions between the absorbed TEMPO molecules. Notably, the ESR spectra of both Sample **2** + TEMPO and SWCNT + TEMPO thin films exhibit a symmetric lineshape. However, when these thin films are compressed into a thicker film ( $\sim 70$   $\mu\text{m}$ ), the ESR spectrum of Sample **2** + TEMPO displays a Dysonian lineshape. This change suggests that the Dysonian lineshape observed in Figure S19 might be attributed to the skin effect.

To confirm the hypothesis regarding the skin effect, we conducted ESR measurement on Sample **5** thin film discharged to  $-0.1$  (Fig. S20c). As expected, a symmetric Lorentzian lineshape was observed when the film thickness ( $\sim 10$   $\mu\text{m}$ ) remained lower than its skin depth ( $\sim 70$   $\mu\text{m}$ ).

## S5.2 Determination of spin concentration

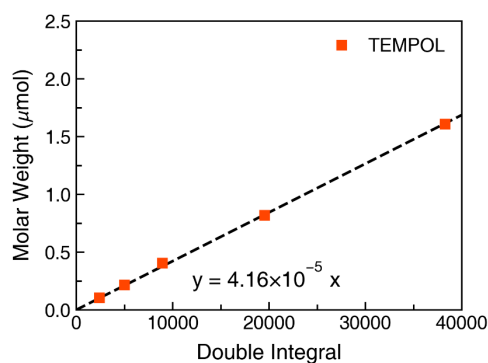


Figure S 21 Double integral of ESR spectrum of TEMPOL/KBr standards.

Sample	Double Integral	Molar weight ( $\mu\text{mol}$ )	Number of spins ( $\mu\text{mol}$ )	Spin concentration (spin/Trip-Phz)
2	5188	0.76	0.22	28.9%
3	6330	1.23	0.26	21.1%
4	4731	1.16	0.20	17.2%
5	7751	2.28	0.32	14.1%

Table S 4 Spin concentration for Samples 2-5 discharged to  $-0.1$  V.

Figure S21 presents the double integral of the ESR spectrum obtained for a series of TEMPOL/KBr samples (one unpaired electron per TEMPOL molecule). Since the ESR signal intensity is directly proportional to the concentration of radicals in the sample, spin concentration of TEMPOL allows for calibration and determination of the radical concentration in Trip-Phz/SWCNT samples. The relationship between the double integral value and the number of spins can be expressed as:

$$\text{Number of spins } [\mu\text{mol}] = 4.16 \times 10^{-5} \times \text{Double Integral}$$

This relationship was employed to calculate the number of spins and spin concentration for Samples 2-5 (discharged to  $-0.1$  V). The results are shown in Table S4.

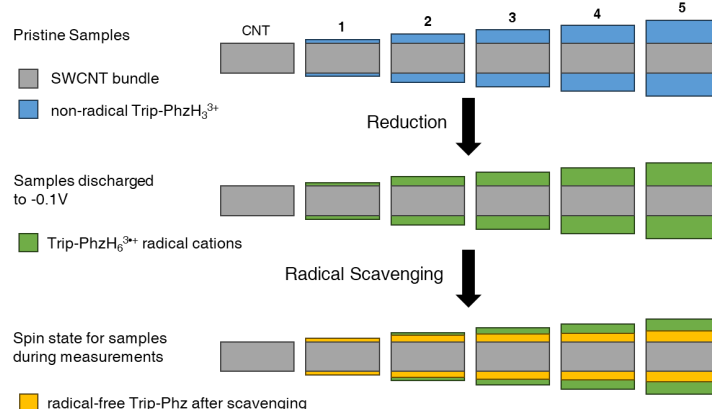


Figure S 22 Schematic illustration possible spin states in Trip-Phz/SWCNT composites for ESR measurements.

Figure S22 depicts a simplified model of the spin states within Trip-Phz/SWCNT composites, relevant for ESR measurements. In their pristine state, all samples are in a close-shell configuration. Upon discharging the samples to  $-0.1$  V, a reduction process occurs. The protonated  $\text{Trip-PhzH}_3^{3+}$  molecules are transformed into the  $\text{Trip-PhzH}_6^{3+}$  radical cations. For samples with a low content of Trip-Phz (such as Sample 2), the model assumes that all the generated  $\text{Trip-PhzH}_6^{3+}$  radicals are scavenged by the SWCNTs. Consequently, no residual unpaired electrons remain within the Trip-Phz layer, leading to a radical-free ESR signal. In contrast, samples with a high content of Trip-Phz (like Samples 3-5) may possess residual  $\text{Trip-PhzH}_6^{3+}$  radicals that are not entirely scavenged by the SWCNTs. The presence of these unpaired electrons contributes to a Dysonian lineshape observed in the corresponding ESR spectra (Fig. S19).

### S5.3 Ex-situ ESR spectra

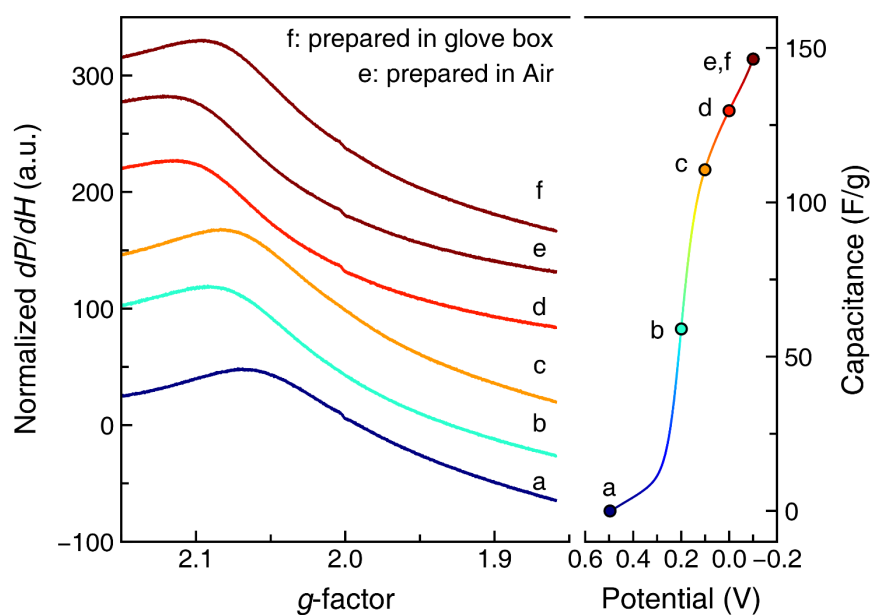


Figure S 23 Ex-situ ESR spectra for electrochemically cycled Sample 1 and the corresponding discharge curve.

The absence of a detectable radical signal for Sample 1 during discharging suggests that sample does not possess unpaired electrons, even though the Trip-PhzH<sub>6</sub><sup>3+</sup> radical was proposed. To exclude potential concerns regarding the oxidation of reduced Trip-Phz during sample preparation in air, an additional experiment was conducted. Sample 1 was cycled and transferred into the ESR tube within an air-free glove box. The ESR spectrum obtained for Sample 1 prepared in the glove box closely resembled the spectrum for the sample prepared in ambient air. This observation strongly suggests that short exposure to air is not the reason for the lack of radicals in Sample 1. Therefore, it is hypothesized that the Trip-Phz radical was scavenged by SWCNT during the electrochemical cycling, owing to the presence of strong  $\pi$ - $\pi$  interactions between Trip-Phz and SWCNT.

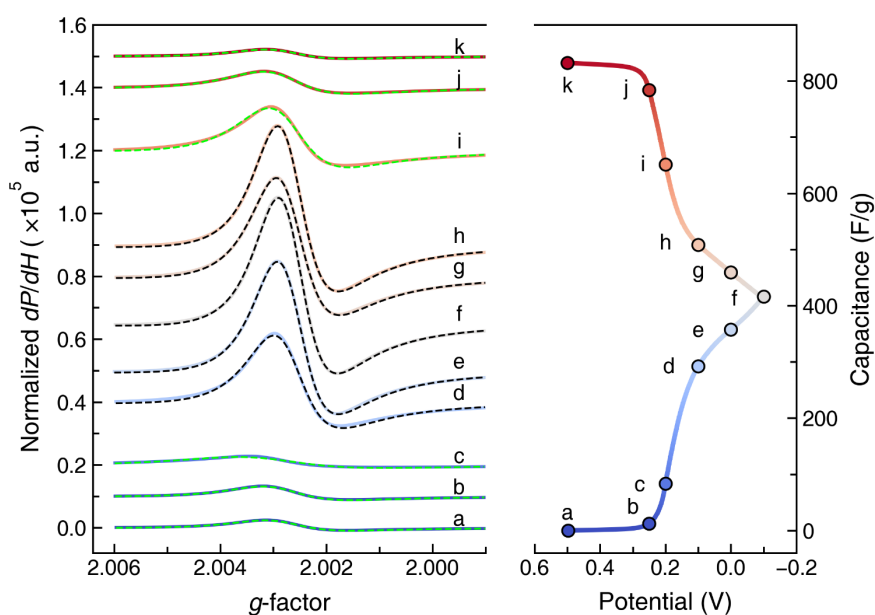


Figure S 24 Ex-situ ESR spectra for Sample 5 during electrochemical cycling and Dysonian line fitting.

Sample	Potential (V)	Capacitance (F/g)	$H_r$ (mT)	$\Delta H_{pp}$ (mT)	$\alpha$	$g$ -factor	Double Integral
a	0.5	0	320.0	0.20	1.00	2.0028	1268
b	0.25	12	320.0	0.21	1.00	2.0029	1382
c	0.2	83	319.9	0.35	1.00	2.0031	2132
d	0.1	292	320.0	0.16	1.00	2.0027	3485
e	0.0	357	319.9	0.15	0.97	2.0027	3828
f	-0.10	416	320.0	0.14	0.97	2.0027	4153
g	0.0	459	319.9	0.15	0.98	2.0027	3740
h	0.1	509	319.9	0.14	1.00	2.0027	3860
i	0.2	651	319.9	0.19	0.97	2.0028	2139
j	0.25	784	319.9	0.21	1.00	2.0028	1418
k	0.5	832	320.0	0.20	1.00	2.0028	729

Table S 5 Dysonian line fitting results of Sample 5 discharged to various potentials.

Figure S24 presents the lineshape analysis of ESR spectra obtained for electrochemically cycled Sample 5, with a molar weight of 1.29  $\mu\text{mol}$ . Notably, all the ESR spectra could be perfectly fitted using a Dysonian function. The parameters obtained from fitting the ESR spectra using the Dysonian function are presented in Table S5.

#### S5.4 Temperature-dependent ESR spectra

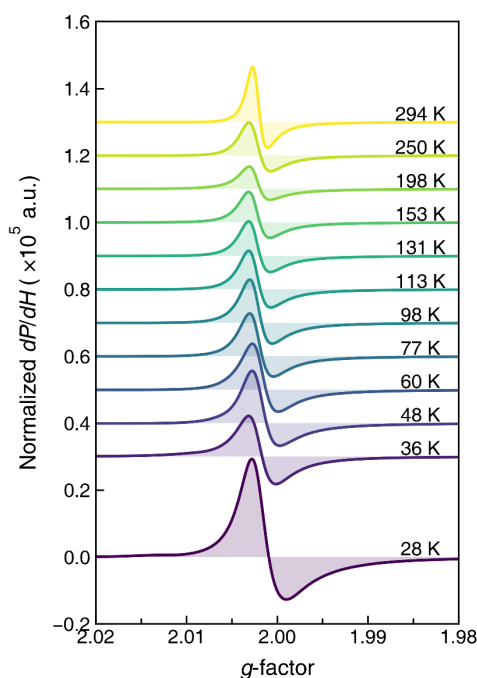


Figure S 25 Temperature-dependent ESR spectra of Sample 5 discharged to  $-0.1\text{V}$ .

Figure S25 presents the ESR spectra of Sample 5 (discharged to  $-0.1\text{V}$ ) recorded at various temperatures, ranging from room temperature down to 28 K. Notably, all the spectra exhibit a Dysonian lineshape suggests high electrical conductivity in the sample. An increase in the peak-to-peak linewidth of the ESR signal with decreasing temperature can be attributed to enhanced dipole-dipole interaction or  $\pi$ - $\pi$  interaction. The spin susceptibility ( $\chi_s$ ) of the sample was determined based on double integral of the corresponding ESR spectra Fig. S25. Figure S26 depicts the normalized  $\chi_s T$  plotted against  $T$ , which follows a modified Curie behavior:  $\chi_s = C/T + \chi_0$ , where  $C$  represents the Curie constant and  $\chi_0$  denotes the temperature-independent component. This observation is in good agreement with the temperature dependence of magnetic susceptibility (Fig. S18). To explain this trend, the following



hypothesis was proposed: upon cooling, the conductivity of the metallic SWCNTs within the composite might increase even though the overall conductivity is hindered by the presence of the less conductive Trip-Phz layer. As the conductivity rises with decreasing temperature, the skin depth might decrease, leading to a reduced number of detectable radicals. The combination of a reduced number of detectable radicals and the Curie behavior of their localized spins can contribute to a temperature-independent term observed in the spin susceptibility. This scenario resembles the behavior of localized spins embedded in a metal, where the temperature independence of the spin susceptibility was observed.<sup>11</sup>

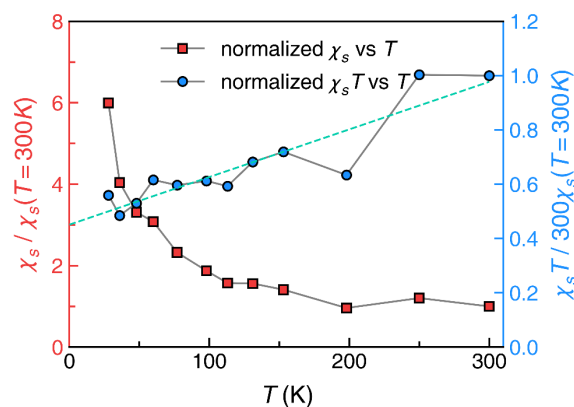


Figure S 26 Temperature dependence of spin susceptibility for Sample 5 discharged to  $-0.1V$ .

## Reference

- 1 R. Ushiroguchi, Y. Shuku, R. Suizu and K. Awaga, *Cryst. Growth Des.*, 2020, **20**, 7593–7597.
- 2 R. Ushiroguchi, R. Suizu, Y. Matsunaga, H. Omachi, Y. Doi, Y. Masubuchi, S. Bandow and K. Awaga, *Chem. Lett.*, 2022, **51**, 1070–1073.
- 3 X. Pu, D. Zhao, C. Fu, Z. Chen, S. Cao, C. Wang and Y. Cao, *Angew. Chem. Int. Ed.*, 2021, **60**, 21310–21318.
- 4 J. Furthmuller, J. Hafner and G. Kresse, *Phys Rev B*, 1994, **50**, 15606.
- 5 G. Kresse and J. Furthmiiller, *Comput. Mater. Sci.*, 1996, **6**, 15.
- 6 P. E. Blochl, *Phys Rev B*, 1994, **50**, 17953.
- 7 J. P. Perdew, K. Burke and M. Ernzerhof, *Physical Review Letter*, 1996, **77**, 3865–3868.
- 8 S. Grimme, J. Antony, S. Ehrlich and H. Krieg, *Journal of Chemical Physics*, 2010, **132**, 154104.
- 9 T. Yumura, N. Sugimori and S. Fukuura, *Phys. Chem. Chem. Phys.*, 2023, **25**, 7527–7539.
- 10 V. Likodimos, S. Glenis, N. Guskos and C. L. Lin, *Phys. Rev. B*, ,
- 11 P. Urban, D. Davidov, ~ B Elschner, T. Plefka and G. Sperlich, *Phys. Rev. B*, 1975, **12**, 75–77.